



Article

Alkali Uranyl Borates: Bond Length, Equatorial Coordination and 5f States

Myrtille O.J.Y. Hunault ^{1,*}, Denis Menut ^{1,†} and Olivier Tougait ^{2,†}

¹ Synchrotron SOLEIL, L'Orme des Merisiers, Saint-Aubin, BP48, 91190 Gif-sur-Yvette, France; denis.menut@synchrotron-soleil.fr

² CNRS, Centrale Lille, University Lille, UMR 8181–UCCS–Unité de Catalyse et Chimie du Solide, F-59000 Lille, France; olivier.tougait@univ-lille.fr

* Correspondence: myrtille.hunault@synchrotron-soleil.fr

† These authors contributed equally to this work.

Abstract: Three uranyl borates, $\text{UO}_2\text{B}_2\text{O}_4$, LiUO_2BO_3 and NaUO_2BO_3 , have been prepared by solid state syntheses. The influence of the crystallographic structure on the splitting of the empty 5f and 6d states have been probed using High Energy Resolved Fluorescence Detected X-ray Absorption Spectroscopy (HERFD-XAS) at the uranium M_4 -edge and L_3 -edge respectively. We demonstrate that the 5f splitting is increased by the decrease of the uranyl U- O_{ax} distance, which in turn correlates with an increased bond covalency. This is correlated to the equatorial coordination change of the uranium. The role of the alkalis as charge compensating the axial oxygen of the uranyl is discussed.

Keywords: uranyl; borate; HERFD-XANES; structure; covalency



Citation: Hunault, M.O.J.Y.; Menut, D.; Tougait, O. Alkali Uranyl Borates: Bond Length, Equatorial Coordination and 5f States. *Crystals* **2021**, *11*, 56. <https://doi.org/10.3390/cryst11010056>

Received: 18 December 2020

Accepted: 8 January 2021

Published: 12 January 2021

Publisher's Note: MDPI stays neutral with regard to jurisdictional claims in published maps and institutional affiliations.



Copyright: © 2021 by the authors. Licensee MDPI, Basel, Switzerland. This article is an open access article distributed under the terms and conditions of the Creative Commons Attribution (CC BY) license (<https://creativecommons.org/licenses/by/4.0/>).

1. Introduction

Uranyl chemistry, which refers to the linear complex ion $[\text{U}^{VI}\text{O}_2]^{2+}$, is rich and has led so far to more than 4000 chemical complexes [1] and more than 350 crystalline structures [2]. This relies mainly on the reactivity in the equatorial plane (perpendicular to trans covalently bounded U-oxo groups) with many types of ligands. Considering oxygen equatorial bonds, the formed uranyl coordination polyhedra are listed as bipyramids with 4, 5 or 6 equatorial ligands, which we will refer to as UO_6 , UO_7 and UO_8 polyhedra respectively. In crystals, UO_7 polyhedra are the most prevalent forms of coordination [2]. Borate uranyl compounds is a family that has received an important interest over the last decade extending from a few first uranyl borates reported [3–8] till more than 50 reported structures today [9–14]. Interestingly, within the uranyl borate family, UO_8 groups are the most prevalent [13,15]. It is argued that the small size of the borate ligand eases the equatorial 6-fold coordination. Would it be only the result of a steric effect? UO_6 and UO_7 groups also occur within the borate family [16]. Comparison between the relatively simple structures of UO_2BO_4 and AUO_2BO_3 (A = alkali ion) shows that despite similar layered structures of uranyl chains, the presence of alkali influences the coordination of the uranyl from UO_8 to UO_7 . The equatorial coordination change of uranyl has also been observed in lithium borate glasses [15]. While the idea of an inert axial oxygen of the uranyl persists until today [17], the reactivity of the axial oxygen has been an increasing subject of research [18] and subsequent evidences have been reviewed for instance by Fortier and Hayton [19]. In particular, interactions with the axial oxygen atoms and alkalis are already found in simple crystalline compounds such as Li_2UO_4 , Na_2UO_4 , $\text{K}_2\text{U}_2\text{O}_7$, and AEUO_4 (AE = Mg, Ca, Sr, Ba) [19].

This study aims at probing the influence of the equatorial coordination shell and determining the effect of the nature of the alkali counterion in contact with the axial oxygen of the uranyl on the 5f electronic structure and on the uranyl trans-dioxo bond covalency. To serve this goal, we chose the relatively simple and wellknown UO_2BO_4 and AUO_2BO_3

($A = \text{Li}$ and Na) uranyl borate compounds and we report their synthesis and spectroscopic study. We used X-ray Absorption Near Edge Spectroscopy (XANES) to determine the influence of the uranyl local structure on the 5f and 6d empty levels and to provide for the first time the unequivocal proof of the relation between both. So far, there has been an important amount of experimental and theoretical work demonstrating the relation between the uranyl bond length and uranium L_3 -edge absorption spectra [15,20–23]. The correlation with the number of equatorial oxygens have also been identified [15]. Uranium M_4 -edge absorption spectroscopy has regained a large interest in the last 10 years for the effective increase of the energy resolution provided by the use of an emission spectrometer (High-Energy Resolution Detected Fluorescence, HERFD, mode) and allows revealing numerous sharp features assigned to the empty 5f levels [15,24,25]. It has been essentially used to decipher between oxidation states of uranium [26–28]. Yet among all data published so far, no systematic study of the relationship between the uranyl structure and the spectroscopic properties have been conducted. Here, we used uranium M_4 -edge High Energy Resolved Fluorescence Detected X-ray Absorption Spectroscopy (HERFD-XAS) to evidence the changes in the uranium 5f electronic structure in relation with the atomic structure. After a detailed description of the crystalline structures, the L_3 - and M_4 -edge HERFD-XANES spectra are discussed.

2. Materials and Methods

2.1. Syntheses

The three compounds, $\text{UO}_2\text{B}_2\text{O}_4$ (hereinafter referred to as **UBO**), LiUO_2BO_3 (**LUBO**) and NaUO_2BO_3 (**NUBO**) have been synthesized by solid state syntheses following previous works from Hoekstrea et al. [3] and Gasperin [5–7]. In details, we used U_3O_8 uranium oxide (Orano, nuclear grade), H_3BO_3 (sigma-aldrich, 99.5%), and the respective alkali carbonates (Alfa Aesar, 99% and 99.5% purity for Li and Na carbonates respectively). **Caution!** Although the uranium precursor used contained depleted uranium, standard safety measures for handling radioactive substances must be followed. The following steps are done in a fume hood. For each compound, reactant-grade powders were weighted according to stoichiometric ratios, grounded together in a mortar and pressed into a pellet. The obtained pellet was placed in a alumina crucible and heated 10 hours in a furnace flushed with dry air at 900 °C. Resulting powders show various colors ranging progressively from greenish-grey for **UBO** to yellow for **NUBO** as illustrated in Figure 1. These colors agree with the indications found in earlier works [5–7].

We note that despite several attempts to apply the synthesis routes described by Gasperin, we were not able to obtain large single crystals. Phase purity was confirmed by powder X-ray diffraction (PXRD). Powder X-ray diffraction analyses were carried out on a Bruker D8 advance in the $\theta - \theta$ Bragg-Brentano geometry using a filtered $\text{Cu K}\alpha$ radiation. The diffractograms were collected from 10° to 80° with a 0.2° step and an acquisition time of 0.5 sec. Rietveld refinements (profile and lattice parameters) were performed with the Fullprof Suite based on structural models established by Gasperin [5–7]. Structure drawings were produced using VESTA software [29].

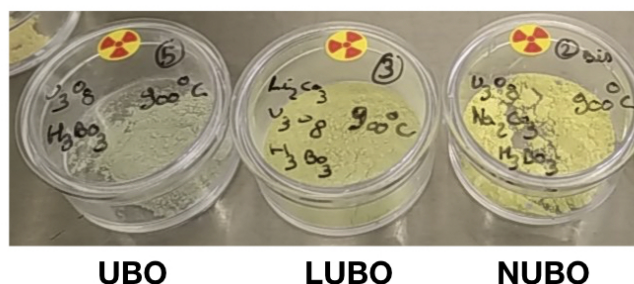


Figure 1. Variation of the color of the obtained powder samples from **UBO** (left) to **NUBO** (right).

2.2. X-ray Absorption Spectroscopy

X-ray absorption spectra were measured at the MARS beamline at the SOLEIL synchrotron (Saint-Aubin, France) [30,31]. The storage ring was operating in top-up mode at an electron current of 500 mA, 2.5 GeV. XAS at the U M_4 -edge (3.7 keV) was measured using the Double Crystal Monochromator (DCM) equipped with a pair of Si(111) crystals. Higher harmonics rejection and vertical focusing was achieved using the Si strip of the two mirrors inserted before and after the DCM with a 4 mrad incidence angle. The incident energy was calibrated using the absorption K-edge of potassium in a KBr pellet (3.6 keV). XAS at the U L_3 -edge (17.2 keV) was measured using the DCM equipped with a pair of Si(220) crystals. Higher harmonics rejection and vertical focusing was achieved using the Pt strip of the two mirrors inserted with a 3.1 mrad incidence angle. The incident energy was calibrated using the absorption K-edge of a yttrium metallic foil (17.038 keV). HERFD-XANES was measured using an emission spectrometer in the Rowland geometry and a KETEK single element silicon solid state detector. The samples were oriented at 45° with respect to the incident beam. For the U M_4 -edge, the $M\beta$ emission line (3.339 keV) was detected, using one Si(220) bent-stripped crystal analyzer with a curvature radius of 1 m. A He-filled chamber was used to reduce the scattering of the emitted x-rays by the air between the sample and the crystal analyzer and the detector. The overall energy resolution of the emission spectrometer was 1.6 eV as determined from the FWHM of the elastic scattering peak at double energy. The spectra were normalized to the maximum of the white-line. For the U L_3 -edge, the $L\alpha_1$ emission line (13.614 keV) was detected, using one Ge(111) bent-stripped crystal analyzer with a curvature radius of 1m. The overall energy resolution of the emission spectrometer was 1.3 eV. The spectra were normalized to an absorption step of 1. All measurements were performed at room temperature. XANES spectra normalization was performed using LARCH software [32].

3. Results

3.1. Uranyl Borate Structures

3.1.1. UBO

$UO_2B_2O_4$ (**UBO**) crystallizes in the monoclinic $C2/c$ space group (Table 1) in agreement with the structure published by Gasperin [5]. A low temperature polymorph has been described by Wang et al. [10] Both polymorphs differ by a 180° rotation of the neighbouring 2D layers called rotational polytypism. The **UBO** structure in our study is sometimes referred to as β - $UO_2B_2O_4$, which is the high temperature polymorph. **UBO** is composed of layers made of linear chains of edge-sharing 6-fold coordinated uranyl (UO_8 groups) linked together by BO_3 units (Figure 2). Each equatorial oxygen is 3-fold coordinated: four are linked to the neighboring uranyl and one boron and two are linked to two borons. The latter are the further away from the uranium (2.61 Å). The chains are staggered one with respect to the other. The resulting planes are also packed in staggered rows such as each uranyl oxygen is directed toward the boron atom of the BO_3 units. The bond lengths of the uranyl polyhedron agrees with typical values for 6 equatorial oxygens (Table 1) [2,15].

3.1.2. LUBO

$LiUO_2BO_3$ (**LUBO**) crystallizes in the monoclinic $P2_1/c$ space group (Table 1) in agreement with the structure published by Gasperin [7]. **LUBO** is composed of chains of edge-sharing 5-fold coordinated uranyl (UO_7 groups). Because of the 5-fold equatorial coordination, the chains form a zig-zag. The equatorial oxygens of the uranyl are all but one 3-fold coordinated to two uranyl and one boron (Figure 2). The fifth equatorial oxygen is only bound to one single boron. The chains are connected together by BO_3 units and form a concerted plain very different from the flat layers found in **UBO**. The layers are perfectly aligned and in-between each layer are the alkali ions. The alkali is found in a site formed by two uranyl oxygens and two 2-fold equatorial oxygens. Table 1 shows that the decrease of the equatorial coordination from 6 to 5 is correlated with the increase of the $U-O_{ax}$ bond distance and the decrease of the $U-O_{eq}$ average bond distance.

These distances are consistent with the trend observed in uranyl oxide compounds [2] and borates in particular [15]. The lithium counterion is placed in between the uranyl layers in contact with four oxygens from four different uranyl polyhedrons at distances ranging from 1.92 Å and 2.09 Å: two equatorial oxygens bonded to borons and two axial oxygens.

Table 1. Crystallographic data for $\text{UO}_2\text{B}_2\text{O}_4$ (**UBO**), LiUO_2BO_3 (**LUBO**) and NaUO_2BO_3 (**NUBO**).

Compound	UBO	LUBO	NUBO
formula	$\text{UO}_2\text{B}_2\text{O}_4$	LiUO_2BO_3	NaUO_2BO_3
color	greyish-green	dark yellow	yellow
space group	mono C2/c	$P2_1/c$	Pcam
a (Å)	12.515 (1)	5.772 (1)	10.735 (1)
b (Å)	4.189 (1)	10.581 (1)	5.788 (1)
c (Å)	10.478 (1)	6.838 (1)	6.869 (1)
α (deg)	90	90	90
β (deg)	122.21 (1)	105.02 (1)	90
γ (deg)	90	90	90
V (Å ³)	464.73 (1)	403.38 (1)	426.79 (1)
Bond distances * (Å)			
U-O _{ax}	1.762 (9)	1.787 (20)	1.807 (12)
U-O _{ax}	1.762 (9)	1.801 (20)	1.810 (13)
U-O _{eq}	2.382 (6)	2.282 (20)	2.273 (10)
U-O _{eq}	2.382 (6)	2.294 (20)	2.303 (9)
U-O _{eq}	2.497 (6)	2.344 (20)	2.303 (9)
U-O _{eq}	2.497 (6)	2.398 (20)	2.411 (8)
U-O _{eq}	2.610 (6)	2.411 (20)	2.411 (8)
U-O _{eq}	2.610 (6)	-	-

* Based on the new lattice parameters; the standard deviations are from References [5–7].

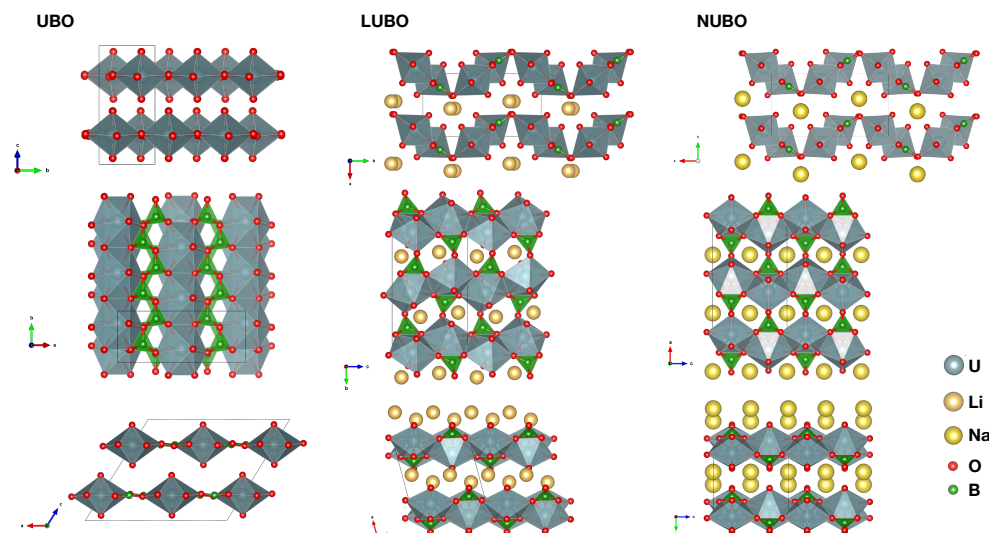


Figure 2. Views of the crystal structures of **UBO**, **LUBO** and **NUBO**.

3.1.3. NUBO

NaUO_2BO_3 (**NUBO**) crystallizes in the orthorhombic Pcam space group (Table 1) in agreement with the structure published by Gasperin [6]. Similarly to **LUBO**, **NUBO** is composed of zig-zag chains of edge-sharing 5-fold coordinated uranyl. These chains are connected together by BO_3 groups to form concertinaed plains (Figure 2). The layers are perfectly superimposed and in-between each layer are the alkali ions. The alkali is found in a site formed by two uranyl oxygens and two 2-fold equatorial oxygens. The subtle difference between **LUBO** and **NUBO** is observed in the position of the alkali cations, the

angle between the equatorial planes of the uranyl chains and the uranyl bond lengths. The change from lithium to sodium also modifies slightly the bond lengths resulting in a very light increase of the $U-O_{ax}$ bond distance and decrease of the $U-O_{eq}$ average bond distance (Table 1). The sodium counterion is placed between the layers and aligned in channels. Within c.a. 2.4 Å, it is in contact with two equatorial boron-bounded oxygens from two different uranyles from one layer and two axial oxygens from two other uranyl of the other layer. Two other axial oxygens are at a distance of 2.89 Å.

3.2. X-ray Absorption Spectroscopy

Uranium L_3 -edge XANES spectra have been used successfully to identify the uranyl structure [20,22,23]. Figure 3 compares the HERFD-XANES spectra at U L_3 -edge of the three compounds **UBO**, **LUBO** and **NUBO**. U L_3 -edge spectra are dominated by transitions to the empty 6d-levels of uranium. All three spectra have similar typical shapes of uranyl compounds: the effective high energy resolution provided by the emission spectrometer reveals a pre-edge feature (P) at 17.166 keV assigned to the empty 5f-levels, [33] then an intense white line (WL) at 17.1735 keV followed by two features (A) and (B) at 17.186 keV and 17.214 keV respectively, characteristic from uranyl species [21–23]. The comparison between the three compounds reveals that the position of feature (A) shifts to lower energies and the position of feature (B) shifts to higher energies when changing from **UBO** to **LUBO** to **NUBO**. These features are assigned to multiple scattering (MS) features from the uranyl polyhedron and their shifts have been assigned to the change of the uranyl polyhedron distances: feature (A) is assigned to the MS resonance from the axial oxygen and feature (B) is assigned to the equatorial oxygens [15,20,21,34,35]. The inverse relation between the relative energy position of the features and the bond length has been investigated by several authors, both experimentally by comparing different compounds [20] and theoretically based on FEFF calculations [23]. The present data follow these trends. In summary, the U L_3 -edge HERFD-XANES spectra show changes resulting from the uranium-oxygen bond distances associated with the conversion from UO_8 to UO_7 polyhedrons.

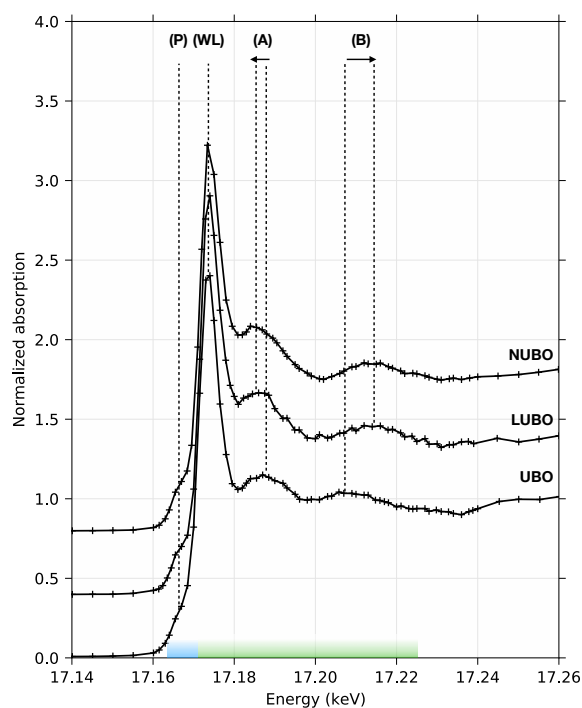


Figure 3. High Energy Resolved Fluorescence Detected X-ray Absorption Spectroscopy (HERFD-XAS) spectra at the U L_3 -edge, from **UBO** (bottom) to **NUBO** (top).

HERFD-XANES at U M_4 -edge probes the empty 5f-levels of uranium. We observe that the modification of the uranyl bond length is correlated with a modification of the spectral shape. Typical HERFD-XANES spectra of uranyl species are observed for all three compounds (Figure 4): the spectra split into three main features [15]. In a molecular orbital model of the uranyl, these features are assigned to electronic transitions to empty non-bonding and anti-bonding 5f levels (Figure 5) [36]. The white line (a) and its shoulder (a') are assigned to the non-bonding $5f\delta/\phi_u$ levels, feature (b) is assigned to the anti-bonding $5f\pi_u^*$ level and feature (c) is assigned to the anti-bonding $5f\sigma_u^*$ level [24,25,37]. We observe that the splitting between the features decreases when changing from **UBO** to **LUBO** to **NUBO** in this order, revealing the stabilisation of the anti-bonding molecular orbitals. Although several factors can influence the uranyl 5f splitting, (e.g., nature of the equatorial ligands, uranyl bending) here, the first major structural change from **UBO** to **LUBO** is a shift from 6 to 5-fold equatorial coordination (from UO_8 to UO_7 polyhedrons) in correlation with the increase of the two $U-O_{ax}$ bond length (plus 0.025 Å and plus 0.038 Å, see Table 1). The decrease of the energy of HERFD-XANES features reflects a stabilisation of the 5f empty levels, which in turn can be assigned to a decrease of the uranyl bond covalency. This result confirms previous inferences proposed in the case of lithium borate glasses [15].

Comparison between **LUBO** and **NUBO** is further interesting as it shows a difference despite only slight structural changes (plus 0.020 Å and plus 0.009 Å for the axial oxygens and minus 0.01 Å on average for the equatorial oxygens, see Table 1). A small energy shift of the spectral features is observed. These results confirm that the energy splitting of the empty 5f levels, probed by U M_4 -edge HERFD-XANES is very sensitive on the axial and equatorial uranyl bond distances.

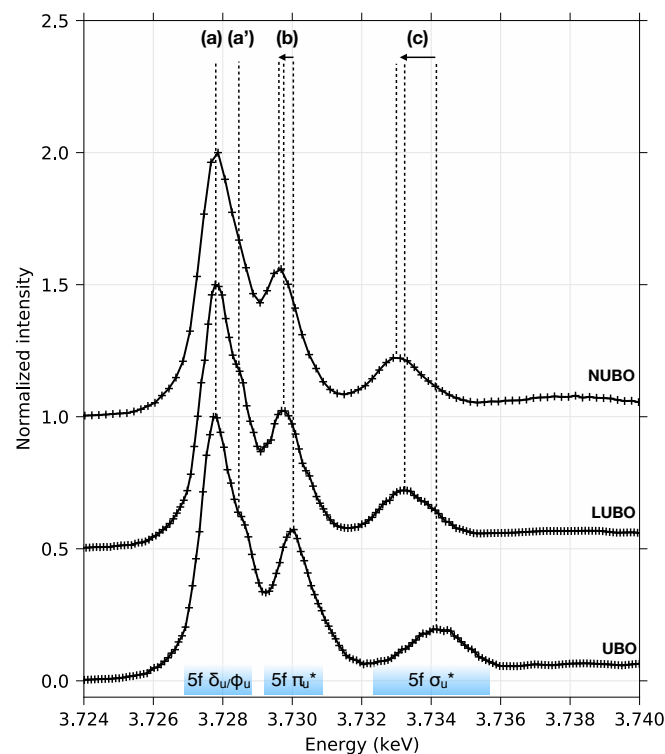


Figure 4. HERFD-XANES spectra at the U M_4 -edge, from **UBO** (bottom) to **NUBO** (top).

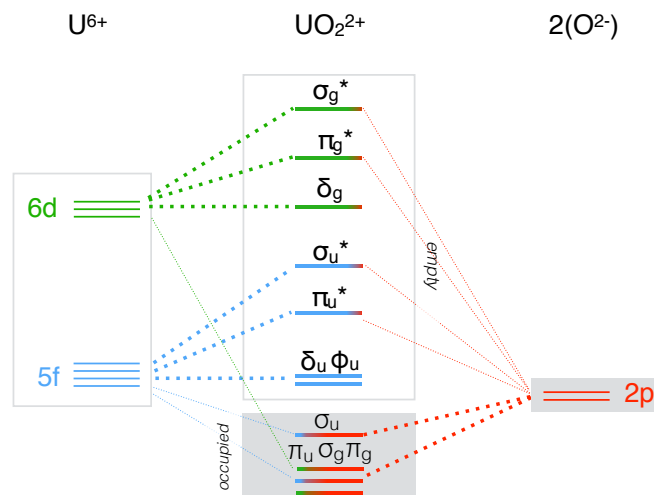


Figure 5. Proposed molecular orbital diagram of the uranyl species adapted from Reference [36].

4. Discussion

The equatorial coordination decrease observed when changing from **UBO** to **LUBO**, can be seen as analogous with the behavior of divalent transition metal ions in alkali borate glasses [38,39] and uranyl in lithium borate glasses [15]: the addition of alkalis to the borate glass induces the decrease of the coordination number of 3d ions and uranyl. However, contrary to borate glasses, here in the studied crystals the presence of alkalis does not result in the coordination change of boron from triangular to tetrahedral [39–41]. Similar trend is found in crystalline lithium borate compounds [42]. The addition of alkalis results in the change of the crystal structure and the uranyl coordination. The nature of the alkali is also important. Comparison between **LUBO** and **NUBO** shows slight uranyl polyhedron changes together with small changes in the crystal structure. Similarly, in high-alkali borate glasses, it has been shown that the bigger the alkali, the shorter the transition metal-oxygen bond and the lower the coordination number [39]. Altogether, these results confirm the similar behaviour of transition metal ions and uranyl ions with respect to the neighbouring cation field strength. In light of the Pauling's second rule, we can suggest that the presence of the alkali counterion in contact with the axial oxygen of the uranyl agrees with the increased U-O_{ax} distance. Although considered as inert for a long time, the uranyl axial oxygen has shown the ability toward oxo-functionalisation in specific complexes including in particular silylation reactions. Li and K cations are used in these reactions to activate the uranyl bond [18]. Here, the structural similarities between **LUBO** and **NUBO** (same equatorial ligands) highlight that the change in the nature of the alkali correlates with the change in the splitting of the 5f empty levels. The U M₄-edge HERFD-XANES spectra provide a direct evidence of this effect.

5. Conclusions

Crystal structure and spectroscopic data of **UBO**, **LUBO** and **NUBO** have been compared. U L₃-edge and U M₄-edge HERFD-XANES probe respectively the empty 6d and 5f levels and reveal the correlation between the atomic and the electronic structures. While the changes of the U L₃-edge spectral shape with the uranyl bond length and equatorial coordination are quite well described, these results provide for the first time the experimental proof of the inverse relationship between the uranyl bond length and the splitting of the empty 5f level. These results will provide precious benchmark data for complementary theoretical calculations of the uranium-oxygen orbital hybridization. Eventually, these results suggest that U M₄-edge HERFD-XANES could be a powerful probe of the electronic origin of the uranyl reactivity and distortions.

Author Contributions: All authors contributed equally to this work. All authors have read and agreed to the published version of the manuscript.

Funding: This research received no external funding.

Institutional Review Board Statement: Not applicable.

Informed Consent Statement: Not applicable.

Data Availability Statement: The data presented in this study are available on request from the corresponding author.

Acknowledgments: We thank SOLEIL synchrotron facility for providing beamtime. We thank Alexandre Rolland for his help in preparing the samples.

Conflicts of Interest: The authors declare no conflict of interest.

References

1. Hayton, T.W. Understanding the origins of $O_{yl}-U-O_{yl}$ bending in the uranyl (UO_2^{2+}) ion. *Dalton Trans.* **2018**, *47*, 1003–1009. [[CrossRef](#)]
2. Burns, P.C. U^{6+} minerals and inorganic compounds: insights into an expanded structural hierarchy of crystal structures. *Can. Mineral.* **2005**, *43*, 1839–1894. [[CrossRef](#)]
3. Hoekstra, H.R. Uranyl Metaborate and Sodium Uranyl Borate. In *Lanthanide/Actinide Chemistry*; Fields, P.R., Moeller, T., Eds.; Series Title: Advances in Chemistry; American Chemical Society: Washington, DC, USA, 1967; Volume 71, pp. 320–330. [[CrossRef](#)]
4. Behm, H. Hexapotassium (cyclo-octahydroxotetracosaoxohexadecarborato)dioxouranate(VI) dodecahydrate, $K_6[UO_2B_{16}O_{24}(OH)_8] \cdot 12H_2O$. *Acta Crystallogr. Sect. Cryst. Struct. Commun.* **1985**, *41*, 642–645. [[CrossRef](#)]
5. Gasperin, M. Structure du borate d'uranium UB_2O_6 . *Acta Crystallogr. Sect. C* **1987**, *43*, 2031–2033. [[CrossRef](#)]
6. Gasperin, M. Synthèse et structure du borouranate de sodium, $NaBUO_5$. *Acta Crystallogr. Sect. C Cryst. Struct. Commun.* **1988**, *44*, 415–416. [[CrossRef](#)]
7. Gasperin, M. Synthèse et structure du borouranate de lithium $LiBUO_5$. *Acta Crystallogr. Sect. C* **1990**, *46*, 372–374. [[CrossRef](#)]
8. Popa, K.; Beneš, O.; Staicu, D.; Griveau, J.C.; Colineau, E.; Seibert, A.; Colle, J.Y.; Stohr, S.; Raison, P.E.; Somers, J.; et al. Heat capacity, thermal expansion, and thermal diffusivity of $NaUO_2BO_3$. *J. Therm. Anal. Calorim.* **2018**, *132*, 343–351. [[CrossRef](#)]
9. Wang, S.; Alekseev, E.V.; Stritzinger, J.T.; Depmeier, W.; Albrecht-Schmitt, T.E. Crystal Chemistry of the Potassium and Rubidium Uranyl Borate Families Derived from Boric Acid Fluxes. *Inorg. Chem.* **2010**, *49*, 6690–6696. [[CrossRef](#)]
10. Wang, S.; Alekseev, E.V.; Stritzinger, J.T.; Depmeier, W.; Albrecht-Schmitt, T.E. How are Centrosymmetric and Noncentrosymmetric Structures Achieved in Uranyl Borates? *Inorg. Chem.* **2010**, *49*, 2948–2953. [[CrossRef](#)]
11. Wang, S.; Alekseev, E.V.; Ling, J.; Liu, G.; Depmeier, W.; Albrecht-Schmitt, T.E. Polarity and Chirality in Uranyl Borates: Insights into Understanding the Vitrification of Nuclear Waste and the Development of Nonlinear Optical Materials. *Chem. Mater.* **2010**, *22*, 2155–2163. [[CrossRef](#)]
12. Wang, S.; Villa, E.M.; Diwu, J.; Alekseev, E.V.; Depmeier, W.; Albrecht-Schmitt, T.E. Role of Anions and Reaction Conditions in the Preparation of Uranium(VI), Neptunium(VI), and Plutonium(VI) Borates. *Inorg. Chem.* **2011**, *50*, 2527–2533. [[CrossRef](#)] [[PubMed](#)]
13. Wang, S.; Alekseev, E.V.; Stritzinger, J.T.; Liu, G.; Depmeier, W.; Albrecht-Schmitt, T.E. Structure-Property Relationships in Lithium, Silver, and Cesium Uranyl Borates. *Chem. Mater.* **2010**, *22*, 5983–5991. [[CrossRef](#)]
14. Silver, M.A.; Albrecht-Schmitt, T.E. Evaluation of f-element borate chemistry. *Coord. Chem. Rev.* **2016**, *323*, 36–51. [[CrossRef](#)]
15. Hunault, M.O.J.Y.; Lelong, G.; Cormier, L.; Galois, L.; Solari, P.L.; Calas, G. Speciation Change of Uranyl in Lithium Borate Glasses. *Inorg. Chem.* **2019**, *58*, 6858–6865. [[CrossRef](#)] [[PubMed](#)]
16. Pace, K.A.; Koch, R.J.; Smith, M.D.; Morrison, G.; Klepov, V.V.; Besmann, T.M.; Misture, S.T.; zur Loye, H.C. Crystal Growth of Alkali Uranyl Borates from Molten Salt Fluxes: Characterization and Ion Exchange Behavior of $A_2(UO_2)_2B_2O_5$ ($A = Cs, Rb, K$). *Inorg. Chem.* **2020**, *59*, 6449–6459. [[CrossRef](#)] [[PubMed](#)]
17. Neidig, M.L.; Clark, D.L.; Martin, R.L. Covalency in f-element complexes. *Coord. Chem. Rev.* **2013**, *257*, 394–406. [[CrossRef](#)]
18. Baker, R.J. New Reactivity of the Uranyl(VI) Ion. *Chem. Eur. J.* **2012**, *18*, 16258–16271.10.1002/chem.201203085. [[CrossRef](#)]
19. Fortier, S.; Hayton, T.W. Oxo ligand functionalization in the uranyl ion (UO_2^{2+}). *Coord. Chem. Rev.* **2010**, *254*, 197–214. [[CrossRef](#)]
20. Jollivet, P.; Den Auwer, C.; Simoni, E. Evolution of the uranium local environment during alteration of SON68 glass. *J. Nucl. Mater.* **2002**, *301*, 142–152. [[CrossRef](#)]
21. Allen, P.G.; Bucher, J.J.; Clark, D.L.; Edelstein, N.M.; Ekberg, S.A.; Gohdes, J.W.; Hudson, E.A.; Kaltsoyannis, N.; Lukens, W.W.; Neu, M.P.; et al. Multinuclear NMR, Raman, EXAFS, and X-ray diffraction studies of uranyl carbonate complexes in near-neutral aqueous solution. X-ray structure of $[C(NH_2)_3]_6[(UO_2)_3(CO_3)_6] \cdot 6H_2O$. *Inorg. Chem.* **1995**, *19*, 4797–4807. [[CrossRef](#)]
22. Den Auwer, C.; Simoni, E.; Conradson, S.; Madic, C. Investigating Actinyl Oxo Cations by X-ray Absorption Spectroscopy. *Eur. J. Inorg. Chem.* **2003**, *2003*, 3843–3859.10.1002/ejic.200300093. [[CrossRef](#)]
23. Zhang, L.; Zhou, J.; Zhang, J.; Su, J.; Zhang, S.; Chen, N.; Jia, Y.; Li, J.; Wang, Y.; Wang, J.Q. Extraction of local coordination structure in a low-concentration uranyl system by XANES. *J. Synchrotron Radiat.* **2016**, *23*, 758–768. [[CrossRef](#)] [[PubMed](#)]

24. Vitova, T.; Pidchenko, I.; Fellhauer, D.; Bagus, P.S.; Joly, Y.; Pruessmann, T.; Bahl, S.; Gonzalez-Robles, E.; Rothe, J.; Altmaier, M.; et al. The role of the 5f valence orbitals of early actinides in chemical bonding. *Nat. Commun.* **2017**, *8*. [[CrossRef](#)] [[PubMed](#)]
25. Kolorenč, J.; Kvashnina, K.O. Theoretical Modelling of High-Resolution X-Ray Absorption Spectra at Uranium M4 Edge. *MRS Adv.* **2018**, *3*, 3143–3148. [[CrossRef](#)]
26. Kvashnina, K.O.; Butorin, S.M.; Martin, P.; Glatzel, P. Chemical State of Complex Uranium Oxides. *Phys. Rev. Lett.* **2013**, *111*. [[CrossRef](#)]
27. Leinders, G.; Bes, R.; Pakarinen, J.; Kvashnina, K.; Verwerft, M. Evolution of the Uranium Chemical State in Mixed-Valence Oxides. *Inorg. Chem.* **2017**, *56*, 6784–6787. [[CrossRef](#)]
28. Bès, R.; Kvashnina, K.; Rossberg, A.; Dottavio, G.; Desgranges, L.; Pontillon, Y.; Solari, P.L.; Butorin, S.M.; Martin, P. New insight in the uranium valence state determination in $U_yNd_{1-y}O_{2\pm x}$. *J. Nucl. Mater.* **2018**, *507*, 145–150. [[CrossRef](#)]
29. Momma, K.; Izumi, F. VESTA 3 for three-dimensional visualization of crystal, volumetric and morphology data. *J. Appl. Crystallogr.* **2011**, *44*, 1272–1276. [[CrossRef](#)]
30. Sitaud, B.; Solari, P.L.; Schlutig, S.; Llorens, I.; Hermange, H. Characterization of radioactive materials using the MARS beamline at the synchrotron SOLEIL. *J. Nucl. Mater.* **2012**, *425*, 238–243. [[CrossRef](#)]
31. Llorens, I.; Solari, P.; Sitaud, B.; Bes, R.; Cammelli, S.; Hermange, H.; Othmane, G.; Safi, S.; Moisy, P.; Wahu, S.; et al. X-ray absorption spectroscopy investigations on radioactive matter using MARS beamline at SOLEIL synchrotron. *Radiochim. Acta* **2014**, *102*, 957–972. [[CrossRef](#)]
32. Newville, M. Larch: An Analysis Package for XAFS and Related Spectroscopies. *J. Phys. Conf. Ser.* **2013**, *430*, 012007. [[CrossRef](#)]
33. Vitova, T.; Kvashnina, K.O.; Nocton, G.; Sukharina, G.; Denecke, M.A.; Butorin, S.M.; Mazzanti, M.; Caciuffo, R.; Soldatov, A.; Behrends, T.; et al. High energy resolution x-ray absorption spectroscopy study of uranium in varying valence states. *Phys. Rev. B* **2010**, *82*, 235118. [[CrossRef](#)]
34. Petiau, J.; Calas, G.; Petitmaire, D.; Bianconi, A.; Benfatto, M.; Marcelli, A. Delocalized versus localized unoccupied 5f states and the uranium site structure in uranium oxides and glasses probed by X-ray-absorption near-edge structure. *Phys. Rev. B* **1986**, *34*, 7350. [[CrossRef](#)] [[PubMed](#)]
35. Farges, F.; Ponader, C.W.; Calas, G.; Brown, G.E. Structural environments of incompatible elements in silicate glass/melt systems: II. UV, UV, and UVI. *Geochim. Cosmochim. Acta* **1992**, *56*, 4205–4220. [[CrossRef](#)]
36. Denning, R.G. Electronic Structure and Bonding in Actinyl Ions and their Analogs. *J. Phys. Chem. A* **2007**, *111*, 4125–4143. [[CrossRef](#)]
37. Fillaux, C.; Berthet, J.C.; Conradson, S.D.; Guilbaud, P.; Guillaumont, D.; Hennig, C.; Moisy, P.; Roques, J.; Simoni, E.; Shuh, D.K.; et al. Combining theoretical chemistry and XANES multi-edge experiments to probe actinide valence states. *Comptes Rendus Chim.* **2007**, *10*, 859–871. [[CrossRef](#)]
38. Galois, L.; Cormier, L.; Calas, G.; Briois, V. Environment of Ni, Co and Zn in low alkali borate glasses: information from EXAFS and XANES spectra. *J. Non-Cryst. Solids* **2001**, *293–295*, 105–111. [[CrossRef](#)]
39. Hunault, M.O.J.Y.; Galois, L.; Lelong, G.; Newville, M.; Calas, G. Effect of cation field strength on Co^{2+} speciation in alkali-borate glasses. *J. Non-Cryst. Solids* **2016**, *451*, 101–110. [[CrossRef](#)]
40. Bray, P.J. NMR and NQR studies of boron in vitreous and crystalline borates. *Inorg. Chim. Acta* **1999**, *289*, 158–173. [[CrossRef](#)]
41. Wu, J.; Stebbins, J.F. Cation Field Strength Effects on Boron Coordination in Binary Borate Glasses. *J. Am. Ceram. Soc.* **2014**, *97*, 2794–2801. [[CrossRef](#)]
42. Lelong, G.; Cormier, L.; Hennet, L.; Michel, F.; Rueff, J.P.; Ablett, J.M.; Monaco, G. Lithium borate crystals and glasses: How similar are they? A non-resonant inelastic X-ray scattering study around the B and O K-edges. *J. Non-Cryst. Solids* **2017**, *472*, 1–8. [[CrossRef](#)]